



PAPER



Cite this: *Energy Environ. Sci.*,
2024, 17, 5552

Fully exploited imidazolium bromide for simultaneous resolution of cathode and anode challenges in zinc–bromine batteries†

Linyu Hu,^{‡a} Chunlong Dai,^{‡b} Yudong Zhu,^c Xu Hou,^d Zhimeng Liu,^c Xin Geng,^c Hailong Wang,^c Jing Chen,^c Nuo Sun,^c Qinlang Rong,^c Yuhao Zhu,^e Xin He *^c and Yuanjing Lin *^a

Aqueous zinc–bromine (Zn–Br₂) batteries feature operational safety and high-energy and high-power densities, but suffer from polybromide dissolution in the cathode and the low reversibility of Zn metal in the anode. Here, we demonstrate that these challenges can be simultaneously tackled by using a fully exploited imidazolium bromide (MPIBr). An in-depth analysis demonstrates that MPIBr enhances both the reversibility and kinetics of Zn anodes. This enhancement arises from MPI⁺ cations participating in the formation of an H₂O–scarce inner Helmholtz plane, suppressing water-associated side reactions. Additionally, electron-donating Br[−] ions contribute to the Zn²⁺–solvation sheath, forming [Zn(H₂O)₅Br]⁺ that promotes Zn²⁺ migration and faster interfacial kinetics. Furthermore, the robust chelation between the MPI⁺ cation and Br_x[−] species significantly impedes shuttling. Notably, the Br[−] anion and Zn²⁺ cation in the electrolyte can construct a dual-plating Zn–Br₂ battery, eliminating the necessity for active materials on both the cathode and anode. The as-prepared dendrite-free and shuttle-free dual-plating Zn–Br₂ batteries demonstrate stable cycling for 1000 cycles even under 100% depth of discharge. This work deepens the understanding of electrolyte composition on electrode interfaces, driving the advancement of high-performance and cost-effective Zn–halogen batteries.

Received 14th May 2024,
Accepted 19th June 2024

DOI: 10.1039/d4ee02096k

rs.c.li/ees

Broader context

Aqueous zinc-based batteries, featuring natural abundance, eco-friendliness, and intrinsic safety, have emerged as promising candidates for large-scale energy storage. In particular, zinc–bromine (Zn–Br₂) batteries, utilizing liquid bromine as the cathode, have the characteristics of high energy density and high power density. However, challenges such as the dissolution of polybromides in the cathode and the limited reversibility of the Zn anode could lead to a shortened cycle life. Although significant efforts have been undertaken to address the issue of severe polybromide dissolution, the stability of Zn anodes has been overlooked for Zn–Br₂ batteries. Besides, attempts to address polybromide dissolution in the cathode may inadvertently worsen the stability of the Zn anode, while electrolyte additives meant to improve Zn anode reversibility may accelerate polybromide dissolution. Consequently, it is highly desired to simultaneously tackle the challenges on both the Br₂ cathode and the Zn anode through rational modification on electrolytes, yet it is largely unexplored. In this study, these challenges can be simultaneously tackled by using a fully exploited imidazolium bromide. This work provides in-depth insights into the electrode interfaces and promotes the implementation of practical high-performance Zn–halogen batteries.

^a School of Microelectronics, Southern University of Science and Technology, Shenzhen 518055, P. R. China. E-mail: linyj2020@sustech.edu.cn

^b College of Materials Science and Engineering, Sichuan University, Chengdu 610065, P. R. China

^c School of Chemical Engineering, Sichuan University, Chengdu 610207, P. R. China. E-mail: xinhe@scu.edu.cn

^d Department of Chemistry, Ångström Laboratory, Uppsala University, SE-751 21 Uppsala, Sweden

^e School of Chemistry and Chemical Engineering, Beijing Institute of Technology, Beijing 100081, P. R. China

† Electronic supplementary information (ESI) available. See DOI: <https://doi.org/10.1039/d4ee02096k>

‡ The authors contributed equally to the work.

Introduction

Rechargeable aqueous zinc-based batteries are emerging as highly promising candidates for large-scale energy storage, benefiting from the natural abundance, eco-friendliness, intrinsic safety, and high theoretical capacity of zinc anodes.^{1–3} Among cathode materials, the liquid bromine electrode is attractive due to its high specific capacity (335.5 mA h g^{−1}) and high oxidation potential (1.087 V vs. SHE).⁴ Accordingly, aqueous zinc–bromine (Zn–Br₂) batteries hold great promise for large-scale energy storage due to their advantages of high operational safety and

cost-effectiveness.^{5,6} Notably, static Zn–Br₂ batteries have received widespread attention without the need for expensive ion exchange membranes or additional auxiliary equipment such as pumps or pipelines.⁷ However, their practical applications are not achieved due to the challenges on both the cathode and anode. Highly soluble polybromides induce the shuttle effect at the cathode,^{8,9} while the hydrogen evolution reaction (HER) and dendritic growth easily occur at the Zn anode,^{10–15} resulting in poor Coulombic efficiency (CE) and a shortened lifespan.

Current research on Zn–Br₂ batteries predominantly focuses on addressing the issue of severe polybromide dissolution,^{16–18} while the stability of Zn anode is hard to ensure simultaneously. To construct a highly reversible and stable Zn anode, one of the effective approaches to tackle the challenges of Zn anode lies in the modification of electrolyte composites. Various functional additives have been used to inhibit the HER and dendrite growth through constructing an electrostatic protective layer^{19–21} or robust solid electrolyte interphase (SEI)^{22,23} on the Zn anode, introducing a pH buffer zone at the electrode/electrolyte interface^{24,25} and regulating the electric field distribution of electrolyte.²⁶ While these strategies indeed improve the CE and the cycling life of the Zn anode, they typically lead to a reduction in the Zn plating/stripping reaction kinetics, mainly due to the increased interfacial resistance, decreased ion conductivity, or reduced Zn²⁺ ion transfer kinetics.^{27–29} Simultaneously achieving rapid plating/stripping reaction kinetics and reversible Zn anodes is highly desired, but still remains largely unrealized. Besides, attempts to mitigate polybromide dissolution in the cathode may inadvertently worsen issues with the Zn anode. Similarly, electrolyte additives designed to enhance the reversibility of the Zn anode may accelerate polybromide dissolution. Therefore, developing a multifunctional electrolyte component is in great demand to simultaneously address issues with both electrodes. While recent reports have noted the use of dual-functional additives in aqueous Zn–MnO₂ and Zn–I₂ batteries, this concept

is still in its early stages.^{24,30,31} Realizing aqueous Zn–Br₂ batteries with inhibition on dendrite growth and the shuttle effects remains largely unexplored.

Here, we report a fully exploited imidazolium bromide (1-methyl-3-propylimidazolium bromide, denoted as MPIBr) to construct a dendrite-free and shuttle-free dual-plating Zn–Br₂ battery (Fig. 1). MPIBr simultaneously enhances the reversibility and kinetics of Zn anodes. The preferential adsorption of MPI⁺ on the Zn anode promotes its entry into the inner Helmholtz plane (IHP), facilitating the formation of an H₂O-scarce IHP (Fig. 1a). This not only enables dendrite-free Zn deposition, but also acts as a barrier between water molecules and the Zn anode, thereby inhibiting the HER. Consequently, the asymmetric Zn||Cu cells show a long cycling life of 2600 cycles, demonstrating the effective suppression of side effects. Moreover, electron-donating Br[−] ions participate in reconstructing the Zn²⁺-solvation sheath (Fig. 1b), leading to the optimization of electrostatic potential and desolvation energy of the Zn²⁺ solvation structure. This optimized structure significantly enhances the plating/stripping kinetics of the Zn anode. Asymmetric Zn||Cu cells with MPIBr deliver a lower nucleation overpotential (9 vs. 47 mV at 1 mA cm^{−2}) compared to the cells without MPIBr. Furthermore, the strong chelating interaction between MPI⁺ and polybromides (Br_x[−]) effectively inhibits the dissolution of Br_x[−] (Fig. 1c), leading to an enhanced CE and prolonged cycling life of Zn–Br₂ batteries. Significantly, the Br[−] anion in the MPIBr can directly participate in the construction of Zn–Br₂ batteries through an *in situ* dual-plating process (Fig. 1d). The as-constructed dual-plating Zn–Br₂ battery shows a long cycling life of 1000 cycles under 100% depth of discharge for both the cathode and anode, demonstrating that the MPIBr simultaneously enables a highly reversible Br₂ cathode and Zn anode. This work provides an in-depth study on electrode interfaces, opening up a new avenue for efficiently utilizing cations and anions of ionic liquid to construct advanced Zn-halogen batteries.

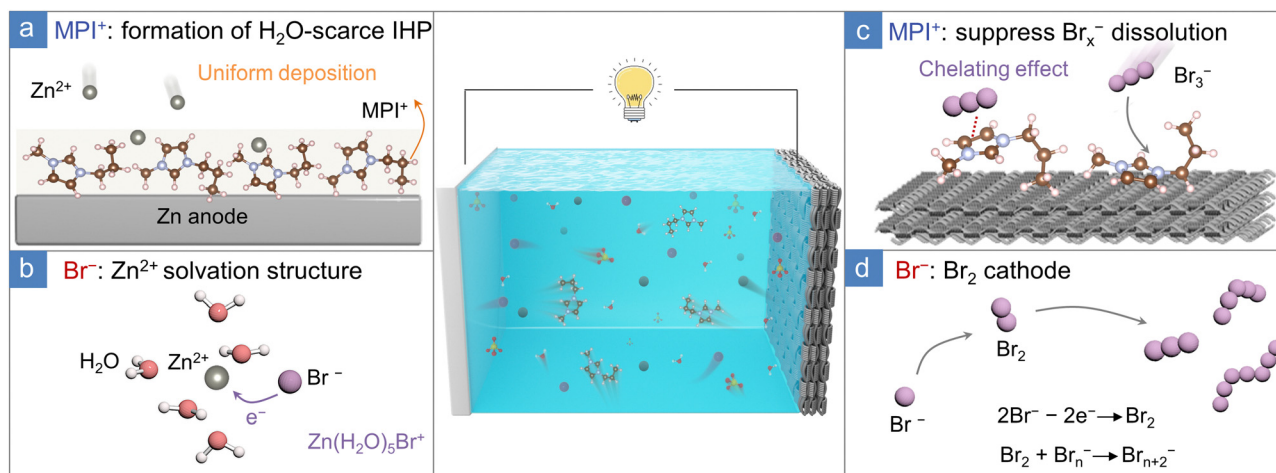


Fig. 1 Fully exploited MPIBr for dendrite-free and shuttle-free dual-plating Zn–Br₂ batteries. The role of MPI⁺ in the (a) formation of an H₂O-scarce IHP on the Zn anode and (c) prevention of the dissolution of polybromides at the cathode. The contribution of Br[−] to (b) the reconstruction of the Zn²⁺ solvation structure for fast kinetics and (d) the bromine source for the *in situ* construction of Br₂ cathode.

Results and discussion

Reversible Zn anode enabled by MPIBr

The electrolytes were prepared by dispersing a certain amount of MPIBr in 1 m (m: mol kg_{H₂O}⁻¹) ZnSO₄ aqueous electrolyte. However, MPIBr is hard to be further dissolved as the concentration reaches 3 m (Fig. S1, ESI[†]). Consequently, electrolytes containing MPIBr at concentrations of 0.5 m, 1 m, and 2 m were examined. The addition of MPIBr has a negligible effect on the pH of the electrolytes (Fig. S2, ESI[†]). Comparative analysis reveals that the introduction of MPIBr results in reduced nucleation overpotentials during the Zn deposition process. In particular, the electrolyte with 2 m MPIBr exhibited the lowest nucleation overpotential, with only 9 mV at 1 mA cm⁻², which is much lower than that of the base electrolyte (47 mV, Fig. S3a, ESI[†]), indicating that a reduced Zn nucleation barrier is obtained with MPIBr. Besides, the observed high reversibility in Zn||Cu cells (Fig. S3b, ESI[†]), coupled with the long-term stability in Zn||Zn cells (Fig. S3c, ESI[†]), emphasizes the advantage of employing the electrolyte containing 2 m MPIBr. Therefore, the optimized formulation of 1 m ZnSO₄ mixed with 2 m MPIBr (ZnSO₄-MPIBr) was employed for further investigation.

To evaluate the Zn plating/stripping reversibility in the electrolytes with and without MPIBr, asymmetric Zn||Cu cells were tested at 2 mA cm⁻² with a capacity of 1 mA h cm⁻². As shown in Fig. 2a, the cell with ZnSO₄-MPIBr operates stably

for more than 2600 cycles and delivers a remarkable average CE of 99.9%, which is among the best compared to other reported works^{21,22,25,32-46} (Fig. 2b and Table S1, ESI[†]). In contrast, the cell in the ZnSO₄ electrolyte fails within 100 cycles with a sharp decline of CE and high polarization (Fig. S4, ESI[†]). The high CE indicates the limited side reactions during Zn plating/stripping processes, which is further proved by PXRD (Fig. S5, ESI[†]) and hydrogen evolution reaction (HER) (Fig. S6a, ESI[†]) tests. Besides, a more positive corrosion potential of the Zn electrode in the ZnSO₄-MPIBr electrolyte demonstrates the heightened corrosion resistance in electrolytes containing MPIBr (Fig. S6b, ESI[†]). Long-term cycling stability in the electrolytes was investigated using Zn||Zn symmetric cells (Fig. S7, ESI[†]). The cell utilizing the ZnSO₄-MPIBr electrolyte demonstrates excellent cycling stability with stable plating/stripping for over 2100 hours, proving a highly reversible Zn plating/stripping process, while those with ZnSO₄ electrolyte suffer from a short circuit after ~120 hours.

The SEM images reveal the evolution insights of the Zn electrode during the plating/stripping processes (Fig. 2c, d and Fig. S8 and S9, ESI[†]). In the ZnSO₄-MPIBr electrolyte, the cycled electrode maintains a flat and dense surface throughout cycling, resulting in extended electrochemical durability. In comparison, the electrode cycled in ZnSO₄ electrolyte exhibits uneven deposition after the 1st plating process, followed by the formation of trenches and pulverized particles in subsequent

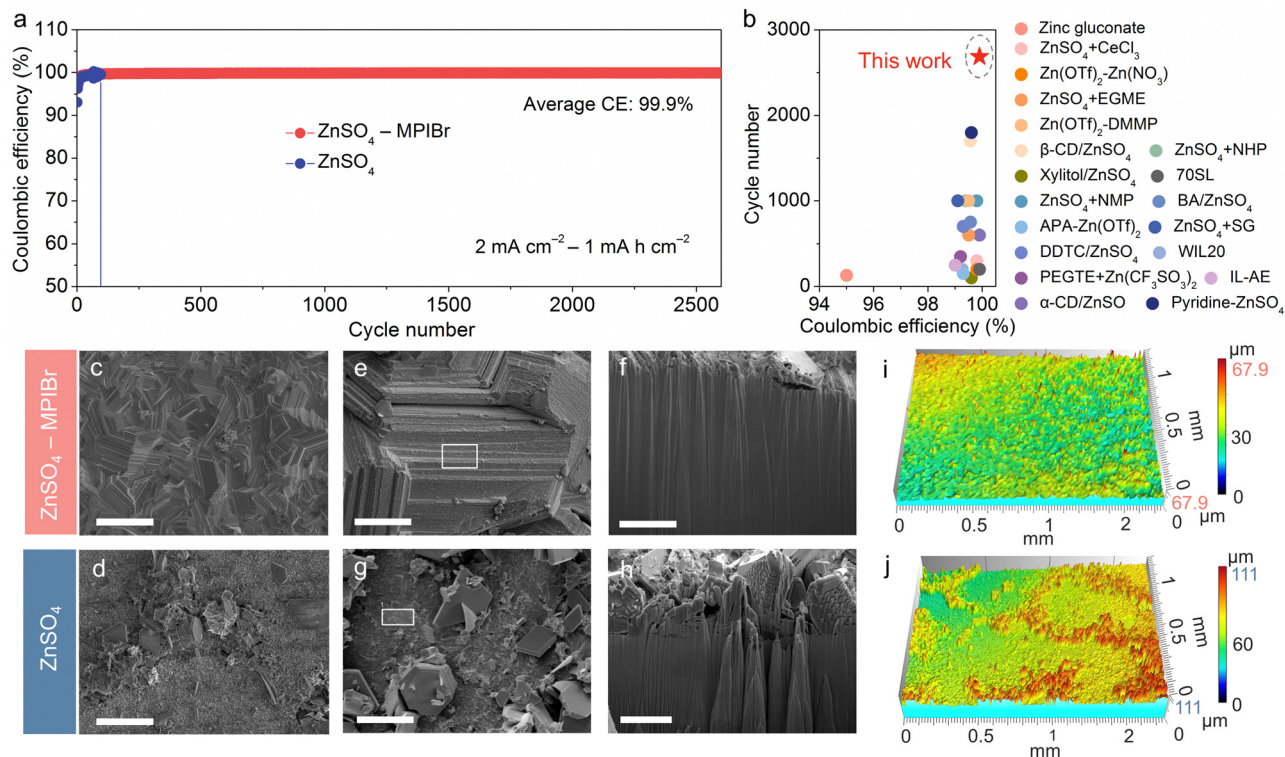


Fig. 2 Electrochemical performance of Zn plating/stripping processes. (a) CE of Zn||Cu cells with different electrolytes. (b) Comparison of the cycle number and CE of Zn||Cu cells with other reported works. SEM images of Zn electrodes after 50 cycles in (c) ZnSO₄-MPIBr and (d) ZnSO₄ electrolytes at 1 mA cm⁻² with 1 mA h cm⁻². Scale bar: 30 μm. FIB-SEM images of a cycled Zn electrode in (e) and (f) ZnSO₄-MPIBr and (g) and (h) ZnSO₄ electrolytes. Scale bar: 5 μm. FIB-etched on the marked area in (e) and (g). 2D confocal images of cycled Zn foils in (i) ZnSO₄-MPIBr and (j) ZnSO₄ electrolytes.

cycles, which adversely affects the electrochemical performance. Focused ion beam (FIB)-SEM images reveal dense and uniform Zn deposition in the ZnSO₄-MPIBr electrolyte (Fig. 2e and f), while loosely and randomly deposited Zn is observed in the ZnSO₄ electrolyte (Fig. 2g and h). 2D confocal microscopy measurements were employed to further confirm the surface topography of the cycled Zn anode (Fig. 2i, j and Fig. S10 and S11, ESI†). The Zn cycled in the ZnSO₄-MPIBr electrolyte exhibits a smooth and uniform surface, featuring a height difference of 67.9 μm. In contrast, the Zn anode cycled in the ZnSO₄ electrolyte displays noticeable protrusions with a height difference of 111.0 μm. The cycled Zn in the ZnSO₄-MPIBr electrolyte also shows high hydrophilicity, which facilitates lowering the interfacial free energy, thus promoting a uniform deposition of Zn (Fig. S12, ESI†). *In situ* optical observation was applied to monitor the Zn deposition process in two types of electrolytes, further demonstrating the uniform Zn deposition in the ZnSO₄-MPIBr electrolyte (Fig. S13, ESI†).

To investigate Zn deposition behavior, XRD patterns of Zn deposition at various times were analyzed to study the evolution of the Zn surface during the stripping/plating process (Fig. S14, ESI†). With increasing deposition time, the intensity of the (002) facet in the ZnSO₄-MPIBr electrolyte gradually increases, suggesting predominant Zn growth along this facet. In contrast, Zn deposition in the ZnSO₄ electrolyte tends to favor the (101) facet, which is prone to dendritic formation.³⁰ These findings suggest that MPIBr promotes specific orientation in Zn deposition, thereby enhancing cycling stability. Accordingly, Zn||Zn cells with ZnSO₄-MPIBr electrolyte exhibit significantly enhanced long-term cycling stability compared to those with ZnSO₄ electrolyte even at high current densities of 5 and 10 mA cm⁻² (Fig. S15a and b, ESI†), surpassing that of most recently reported electrolytes (Fig. S15c and Table S2, ESI†). Furthermore, shelving-recovery tests show the satisfactory cyclic durability of Zn||Zn cells using the ZnSO₄-MPIBr electrolyte, demonstrating their feasible application under practical conditions (Fig. S16, ESI†).

Electrode–electrolyte interface with MPI⁺

The electrode–electrolyte interface is vital for promoting uniform Zn²⁺ deposition and suppressing side reactions. To explore the factors contributing to the uniform Zn deposition in the ZnSO₄-MPIBr electrolyte, the surface chemistry of the cycled Zn anode was evaluated using Ar⁺ sputtering X-ray photoelectron spectroscopy (XPS) depth profiling. The obvious N 1s spectrum signal is ascribed to MPI⁺; nevertheless, with increased sputtering depth, the signal diminishes (Fig. 3a). Besides, the negligible change in reduction current in the Na₂SO₄-MPIBr electrolyte suggests that MPI⁺ remains undecomposed (Fig. S17, ESI†).⁴⁷ These results indicate that MPI⁺ cations have the potential to enter the IHP, leading to the formation of an H₂O-scarce IHP. First-principles calculations were performed to calculate the adsorption energies of MPI⁺ and H₂O on the Zn anode (Fig. 3b). According to the Zn deposition orientation in the ZnSO₄-MPIBr electrolyte (Fig. S14, ESI†), further investigation is directed towards the Zn (002) facet. MPI⁺ exhibits a lower adsorption energy with the Zn (002) facet

compared to H₂O, suggesting that MPI⁺ can be preferentially adsorbed onto the Zn surface. The charge density differences between MPI⁺ and Zn (002) reveal a noticeable electron transfer at the surface, signifying strong electrostatic adsorption.

To further investigate the interface structure of Zn after cycling in the ZnSO₄-MPIBr electrolyte, transmission electron microscopy (TEM) measurements were conducted. The aberration-corrected high-angle annular dark-field scanning (AC-HAADF-STEM) image shows a clear amorphous region on the Zn surface (Fig. 3c). However, the species within the amorphous region are often intricate and challenging to identify.⁴⁸ In this work, near-field infrared nanospectroscopy (nano-FTIR), with a spatial resolution of 10 nm and the ability to detect local molecular composition, was employed to further identify organic species on the Zn surface.⁴⁹ The atomic force microscopy (AFM) and broadband IR “white light” (WL) images illustrate the Zn deposited Cu foil, concomitant with the adsorption of MPI⁺ cations (Fig. 3d). The irregular brightness distribution in the WL image arises from the inconsistent chemical composition at the interface. Increased Zn deposition results in higher conductivity, consequently leading to greater IR reflection. Additionally, enhanced conductivity promotes the deposition of Zn, leading to increased height, which corresponds to the brighter areas in the high-resolution AFM image. Consequently, local nano-FTIR spectra were recorded from the marked brighter regions identified in both the AFM and WL images. As shown in Fig. 3e, the observed peaks at 1610 and 1587 cm⁻¹ are ascribed to the C=C and C=N stretching vibrations in the imidazole (Im) ring, respectively. The peaks at 1460 cm⁻¹ and 1375 cm⁻¹ are ascribed to the δ_{C-H} symmetric bending vibration of alkane, consistent with the characteristics of MPI⁺,^{50,51} further confirming the adsorption of MPI⁺ on the Zn surface.

The distribution of each component was further investigated by time-of-flight secondary-ion mass spectrometry (ToF-SIMS). The 3D elemental distributions indicate that N and C components were primarily enriched on the surface (Fig. 3f and g), with signal intensity gradually decreasing within the detected depth, aligning with the XPS results. During plating, MPI⁺ ions adsorb on the Zn surface, forming an N-rich layer with strong mechanical properties that inhibit water infiltration and promote uniform Zn deposition. Such an interfacial layer can effectively improve the reversibility and long-term stability of Zn deposition (Fig. S18, ESI†).

Reconstruction of the Zn²⁺ solvation structure with Br⁻

To further elucidate the mechanism behind the enhanced stability of the Zn anode with MPIBr, the Zn²⁺ solvation structure in the ZnSO₄-MPIBr electrolyte was first analyzed. As observed in Raman spectra (Fig. S19, ESI†), the addition of MPIBr results in the decreased peak related to the symmetric stretching mode of [Zn(H₂O)₆]²⁺, and the peak associated with the SO₄²⁻ vibration shifts to a lower frequency. Besides, Fourier transform infrared (FTIR) spectra reveal a blueshift in the stretching vibration of SO₄²⁻ after the addition of MPIBr,

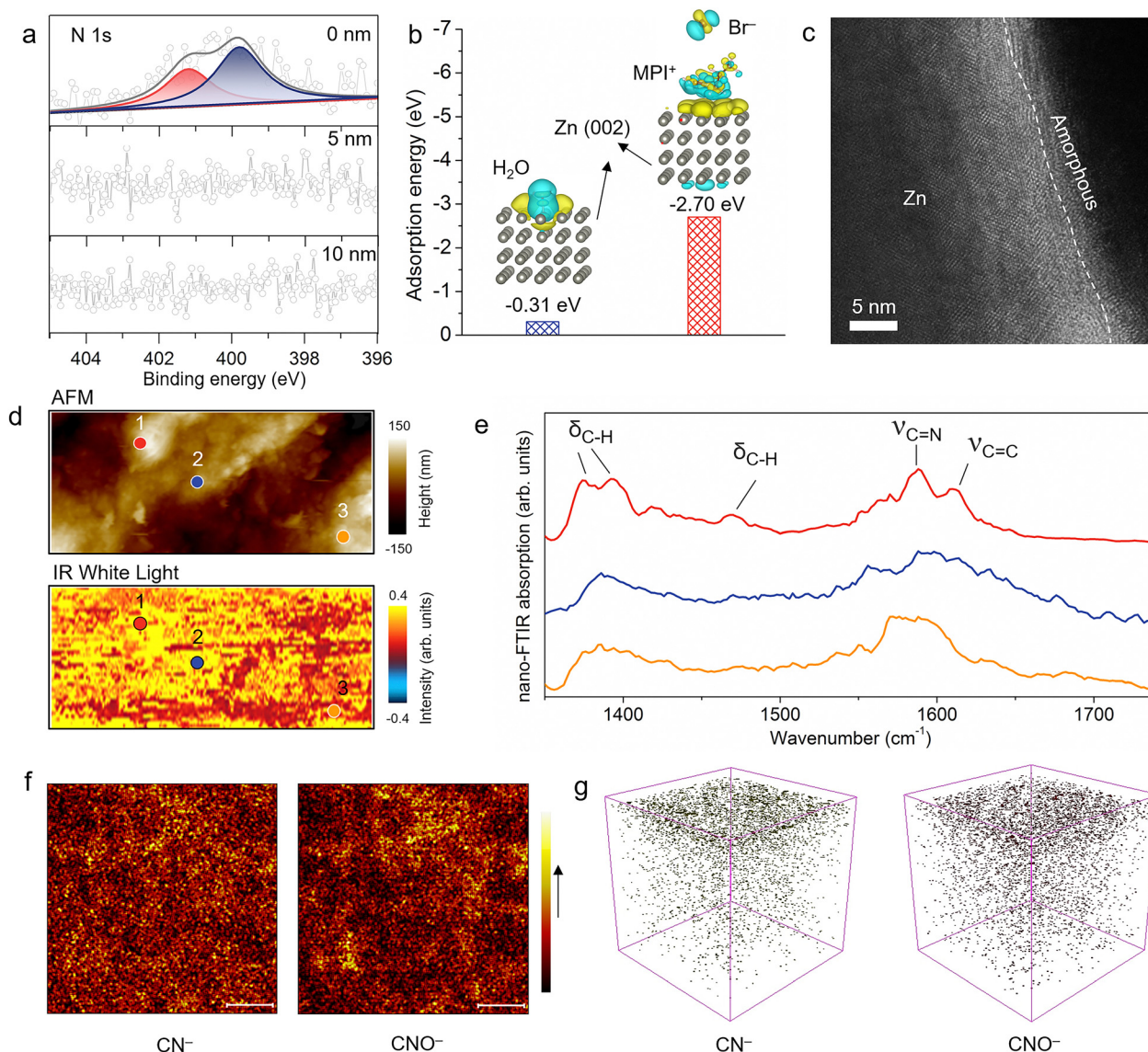


Fig. 3 The detailed structure of the electrode–electrolyte interface. (a) N 1s XPS spectra depth profile of the cycled Zn foil in the ZnSO₄–MPIBr electrolyte. (b) Adsorption energy and differential charge density distributions of H₂O and MPI⁺ on the Zn (002) surface. Key: electron accumulation (yellow) and electron depletion (blue). (c) Aberration-corrected HAADF–STEM images of the cycled Zn in ZnSO₄–MPIBr electrolyte. (d) AFM and IR white light images of the Cu foil after Zn plating. (e) Local nano-FTIR spectra of the Zn surface. (f) Surface mapping (scale bar: 10 μm) and (g) spatial distribution of CN[−] and CNO[−] on cycled Zn detected by ToF–SIMS.

indicating a modification in the solvation structure of Zn²⁺ (Fig. S20, ESI[†]).

X-ray absorption spectroscopy (XAS) measurements were conducted to confirm the local structure of the electrolyte. According to the Zn K-edge X-ray absorption near-edge structure (XANES) spectra (Fig. 4a), the valence state of Zn in the ZnSO₄–MPIBr electrolyte is slightly reduced than that in the ZnSO₄ electrolyte, which could be attributed to the Br[−] coordinated in the solvation structure. The extended X-ray absorption fine structure (EXAFS) spectrum indicates the existence of Zn–Br coordination in the ZnSO₄–MPIBr electrolyte (Fig. 4b), which is consistent with the results observed in the ZnBr₂ solution. The wavelet transform (WT) contour plot also confirms this result (Fig. 4c). The lower electronegativity of Br[−] leads to a

stronger binding energy with Zn²⁺ compared to H₂O (Fig. S21, ESI[†]), thereby facilitating the formation of unique Zn²⁺ solvation structures.

Ab initio molecular dynamics (AIMD) simulation was performed to analyze the Zn²⁺ solvation structure. At the beginning of the simulation, an isothermal–isobaric ensemble (NPT) at 300 K for 10 ps with a 1 fs timestep was applied to ensure the system from AIMD is equilibrated and reliable (Fig. S22, ESI[†]). In the ZnSO₄ electrolyte, the typical solvation structure is composed of Zn²⁺ and six H₂O molecules, with a percentage of 86.1% (Fig. S23 and S24, ESI[†]). However, after the introduction of MPIBr, Br[−] ions partially participate in the Zn²⁺ solvation structure (Fig. 4d). The radial distribution functions (RDFs) for all the possible molecules⁵² around Zn²⁺ confirm

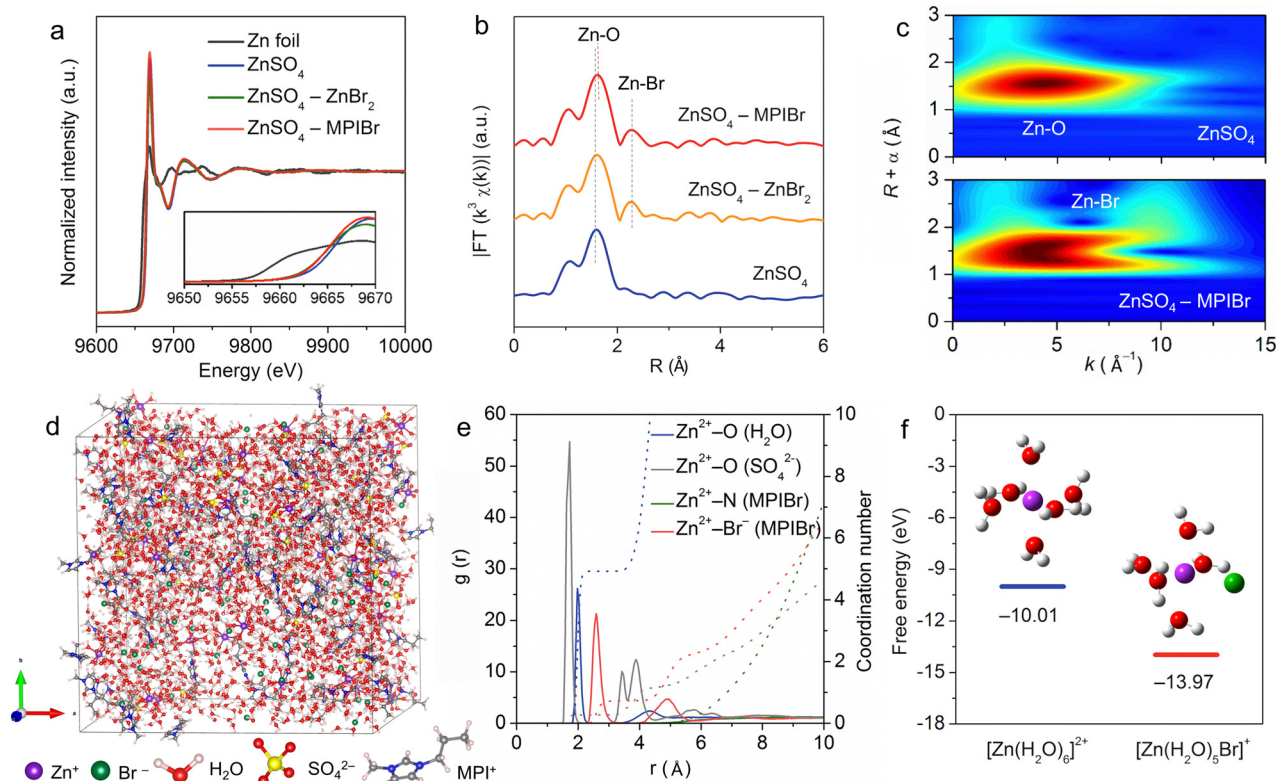


Fig. 4 Structural characterization of the $\text{ZnSO}_4\text{-MPIBr}$ electrolyte. (a) Normalized XANES spectra and (b) Fourier transform EXAFS spectra of the ZnSO_4 , $\text{ZnSO}_4\text{-ZnBr}_2$, and $\text{ZnSO}_4\text{-MPIBr}$ electrolytes. (c) WT contour plots of ZnSO_4 and $\text{ZnSO}_4\text{-MPIBr}$ electrolytes. (d) 3D snapshot of the $\text{ZnSO}_4\text{-MPIBr}$ electrolyte. (e) Radial distribution function and coordination numbers of $\text{Zn}^{2+}\text{-O}(\text{H}_2\text{O})$, $\text{Zn}^{2+}\text{-O}(\text{SO}_4^{2-})$, $\text{Zn}^{2+}\text{-Br}^-(\text{MPIBr})$, and $\text{Zn}^{2+}\text{-N}(\text{MPIBr})$ in the $\text{ZnSO}_4\text{-MPIBr}$ electrolyte. (f) Free energy of different Zn^{2+} solvation structures.

the coexistence of $\text{Zn}^{2+}\text{-O}(\text{H}_2\text{O})$, $\text{Zn}^{2+}\text{-O}(\text{SO}_4^{2-})$, and $\text{Zn}^{2+}\text{-Br}^-(\text{MPIBr})$ in the electrolyte with coordination numbers of 4.95, 0.25, and 0.71, respectively (Fig. 4e). The percentage of H_2O surrounded Zn^{2+} solvation structure decreases to 52.8%, whereas the percentage of Br^- surrounded Zn^{2+} solvation structure reaches 30.5%, suggesting the participation of Br^- ions in the Zn^{2+} solvation structure. These findings are consistent with the Raman, FTIR, and XAS results. Density functional theory (DFT) calculations further confirm that the Br^- surrounded Zn^{2+} solvation structure of $[\text{Zn}(\text{H}_2\text{O})_5\text{Br}]^+$ exhibits the optimal energy configuration with a lower free energy (Fig. 4f).

The reaction kinetics is closely related to the solvation structure of the electrolyte, exerting a pivotal influence on electrochemical reactions. In comparison with $[\text{Zn}(\text{H}_2\text{O})_6]^{2+}$, $[\text{Zn}(\text{H}_2\text{O})_5\text{Br}]^+$ possesses a reduced electrostatic potential (ESP), possibly attributed to the greater electron-donating ability of Br^- ions (Fig. 5a). The lower electrostatic potential (ESP) effectively shields the repulsion between Zn^{2+} ions,^{53,54} thereby promoting the Zn^{2+} migration and transportation (Fig. 5a and Fig. S25, ESI[†]). The time-dependent mean squared displacement (MSD) was employed to analyze the diffusion coefficient of all species (Fig. S26 and S27, ESI[†]). After introducing MPIBr into the ZnSO_4 electrolyte, the diffusion coefficient of Zn^{2+} ions increased from $1.87 \times 10^{-6} \text{ cm}^2 \text{ s}^{-1}$ to $2.59 \times 10^{-6} \text{ cm}^2 \text{ s}^{-1}$, indicating that MPIBr can enhance Zn^{2+} transport due to the

lower ESP of the Br^- surrounded Zn^{2+} solvation structure. Besides, the $\text{ZnSO}_4\text{-MPIBr}$ electrolyte demonstrates the highest ionic conductivity (50 mS cm^{-1}) compared to other electrolytes (Fig. S28, ESI[†]). The solvation structure significantly impacts the desolvation energy. During the plating process, the negative polarization of the Zn surface causes the repulsion of anions, leading to a more facile desolvation process and faster interfacial kinetics (Fig. 5b and c).⁵⁵ Consequently, the activation energy (E_a) was measured by electrochemical impedance spectroscopy (EIS) to evaluate the desolvation energy barrier (Fig. 5d and Fig. S29, ESI[†]). According to the fitting results, the E_a of the $\text{ZnSO}_4\text{-MPIBr}$ electrolyte (28.5 kJ mol^{-1}) is smaller than that of the ZnSO_4 electrolyte (43.6 kJ mol^{-1}), indicating improved ion migration and Zn deposition kinetics.

The $\text{Zn}\|\text{Cu}$ cell with $\text{ZnSO}_4\text{-MPIBr}$ electrolyte exhibits a nucleation overpotential of 9 mV at 1 mA cm^{-2} (Fig. 5e), significantly lower than those of the cell using ZnSO_4 electrolyte (47 mV) and many other reported electrolytes (Fig. S30 and Table S3, ESI[†]). Besides, the $\text{Zn}\|\text{Zn}$ symmetric cell, utilizing the $\text{ZnSO}_4\text{-MPIBr}$ electrolyte, exhibits a lower charge transfer impedance compared to that with the ZnSO_4 electrolyte (Fig. 5f), demonstrating the enhanced reaction kinetics. The rate performances of $\text{Zn}\|\text{Zn}$ and $\text{Zn}\|\text{Cu}$ cells with the $\text{ZnSO}_4\text{-MPIBr}$ electrolyte also demonstrate lower overpotentials under different current densities than those with the ZnSO_4 electrolyte

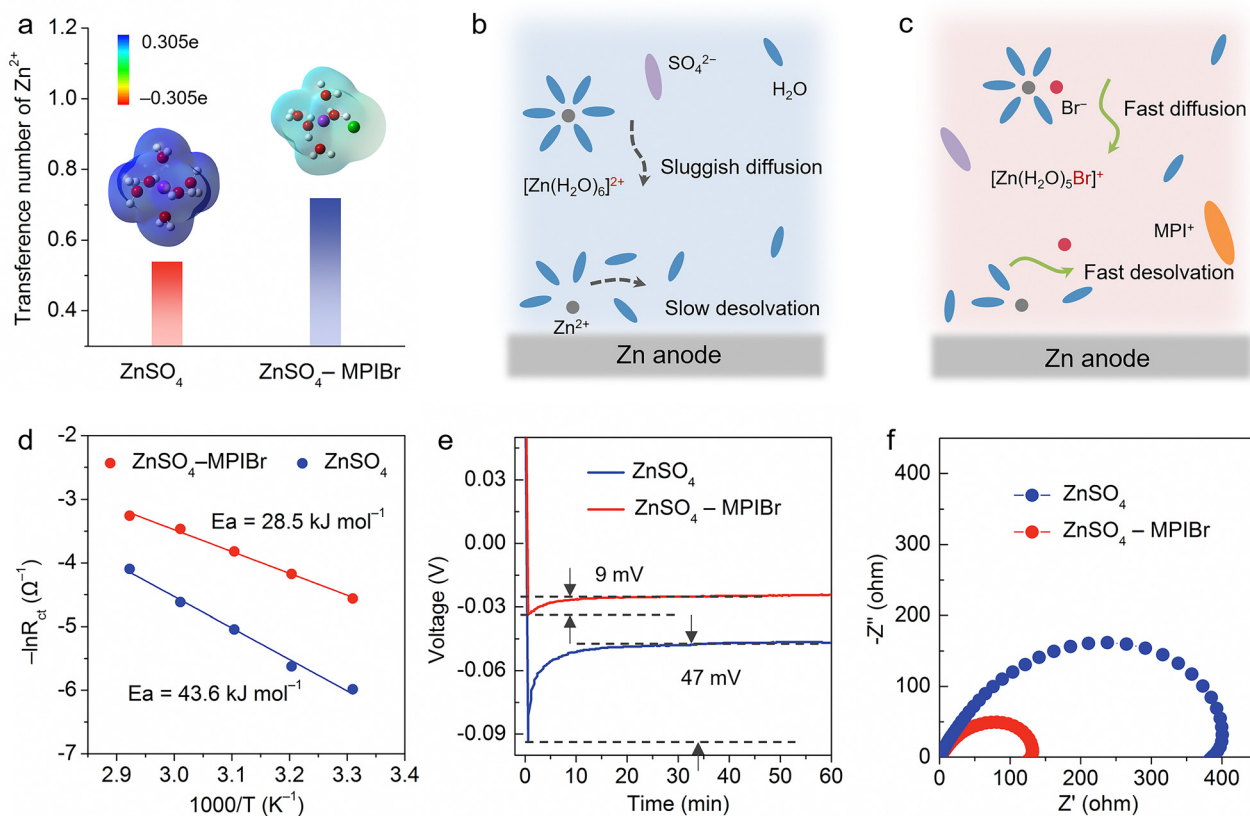


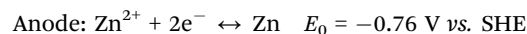
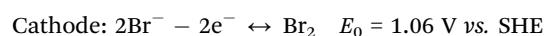
Fig. 5 Reaction kinetics of Zn in the ZnSO_4 -MPIBr electrolyte. (a) Transference number of Zn^{2+} in different electrolytes (inset: electrostatic potential distributions of $[\text{Zn}(\text{H}_2\text{O})_6]^{2+}$ and $[\text{Zn}(\text{H}_2\text{O})_5\text{Br}]^+$). Schematic of diffusion and dissociation of solvated structures in (b) ZnSO_4 and (c) ZnSO_4 -MPIBr electrolytes. (d) Activation energies of Zn||Zn cells. (e) Polarization curves of Zn deposition at 1 mA cm^{-2} with an areal capacity of 1 mAh cm^{-2} . (f) EIS curves of Zn||Zn cells in ZnSO_4 and ZnSO_4 -MPIBr electrolytes.

(Fig. S31–S33, ESI[†]), further confirming the fast kinetics enabled by MPIBr. Besides, the Zn plating/stripping current densities in the electrolytes with and without MPIBr were studied as well. The Zn plating/stripping current densities in the ZnSO_4 -MPIBr electrolyte are much larger than that in the ZnSO_4 electrolyte (Fig. S34, ESI[†]), suggesting that MPIBr accelerates the Zn plating/stripping reaction kinetics. Thus, it can be concluded that MPIBr effectively enhances the reaction kinetics in Zn plating and stripping processes by forming novel solvation structures of $[\text{Zn}(\text{H}_2\text{O})_5\text{Br}]^+$.

Performance and application demonstration of dual-plating Zn–Br₂ batteries

In addition to accelerating Zn plating/stripping reactions and suppressing side reactions, MPIBr can also provide the Br_2 source for *in situ* construction of Zn–Br₂ batteries. The ZnSO_4 -MPIBr electrolyte contains both Br_2 and Zn sources, and a dual-plating strategy was employed to *in situ* construct Zn–Br₂ batteries. During the charging processes, Br^- ions in MPIBr lose electrons, resulting in the generation of Br_2 , which gets deposited on the current collector to form the cathode. Simultaneously, Zn^{2+} ions gain electrons to constitute the Zn anode.

This process is illustrated in Fig. 6a, and the reactions are as follows:



The overall energy density of the Zn–Br₂ batteries is directly influenced by the concentration of Br^- in the electrolyte; a higher Br^- concentration leads to a higher energy density. Accordingly, the ZnSO_4 -MPIBr electrolyte is employed for constructing dual-plating Zn–Br₂ batteries. Cyclic voltammetry (CV) curves demonstrate the successful construction of Zn–Br₂ batteries through the electrolyte (Fig. S35, ESI[†]). The as-fabricated Zn–Br₂ battery delivers a stable cycling performance for 1000 cycles with an average CE of 97.5% at 2 mA cm^{-2} (Fig. 6a). The long cycling life can rival against the best of those reported anode-free Zn-based batteries^{56–64} (Fig. 6b and Table S4, ESI[†]).

Zn–Br₂ batteries typically suffer from a low CE and poor cycling life due to the dissolution of polybromides, whereas batteries utilizing electrolytes containing MPIBr exhibit a high CE (Fig. S36, ESI[†]). To explore the reasons for the high CE in the

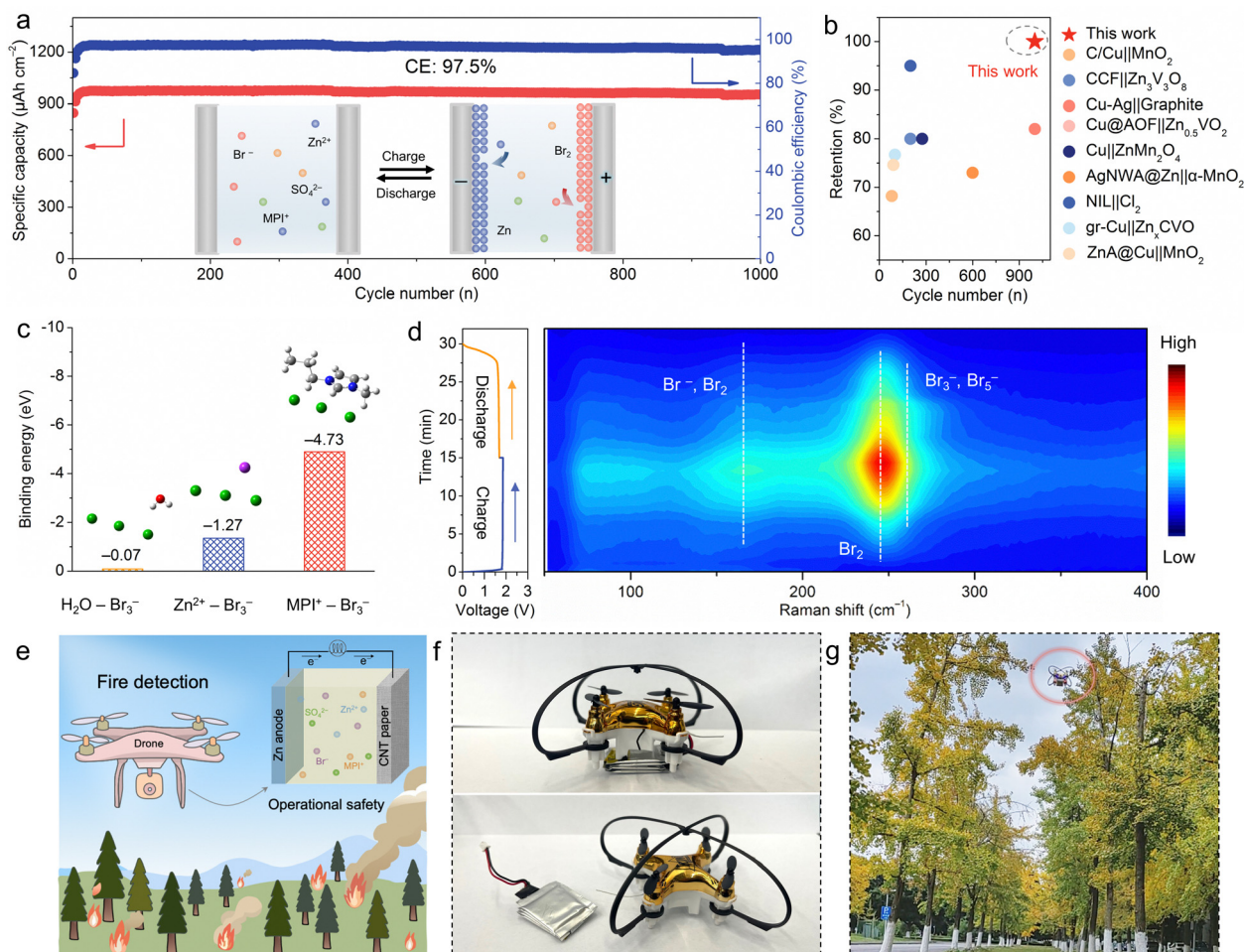


Fig. 6 Electrochemical performances of dual-plating Zn-Br₂ batteries. (a) Cycling performance (inset: schematics of *in situ* construction of the Br₂ cathode and Zn anode during the charging process). (b) Cycling performance compared with other reported anode-free Zn-based batteries. (c) Binding energy of Br₃⁻ with H₂O, Zn²⁺, and MPI⁺. (d) Contour plots of operando Raman patterns from Zn-Br₂ batteries. (e) Illustration showcasing the application of Zn-Br₂ batteries in powering a drone for forest fire detection. (f) Photographs of Zn-Br₂ pouch cells and a small drone. (g) Successful takeoff of the drone powered by Zn-Br₂ pouch cells.

ZnSO₄-MPIBr electrolyte, first-principles calculations were conducted. Br₃⁻ ion is used as the representative of polybromide to study the effect of MPI⁺ on polybromide diffusion. The binding energy between Br₃⁻ and MPI⁺ is lower than that with H₂O or Zn²⁺ (Fig. 6c), signifying the strong chelation of MPI⁺. This chelation effectively inhibits the dissolution of Br_x⁻, contributing to a high CE and long cycling life. *In situ* Raman measurements were employed to further investigate the formation mechanism of the Br₂ cathode (Fig. 6d). During the charging process, the peaks of Br₂ at 249 cm⁻¹ appeared, followed by the appearance of peaks for Br₃⁻ and Br₅⁻ at 257 cm⁻¹. This observation suggests the formation of Br₂ during the dual-plating process, which subsequently combines with Br⁻ ions to form Br_x⁻ ions. CEs at different charge capacities (Fig. S37 and S38, ESI[†]) and different current densities (Fig. S39, ESI[†]) were also evaluated, demonstrating the strong chelation of MPI⁺.

The maximum discharging areal capacity of the Zn-Br₂ batteries was further studied (Fig. S40, ESI[†]), emphasizing

the significance of MPIBr concentration. After charging to 6000 μA h cm⁻², the discharging areal capacity still reaches 5700 μA h cm⁻² with a high CE of 95% in the electrolyte with 2 m MPIBr. To evaluate the practical application, the ZnSO₄-MPIBr electrolyte was employed to assemble the Zn-Br₂ pouch cell, showcasing a substantial discharge capacity of 17 mA h (Fig. S41, ESI[†]). It is worth noting that the electrochemical performances are obtained under 100% depth of discharge for both the cathode and anode.

To demonstrate the promising applications of the as-developed flexible quasi-solid-state Zn-Br₂ batteries, their mechanical robustness and operational safety were validated. The assembled flexible Zn-Br₂ cell shows excellent anti-destructive ability, capable of powering electronic devices after experiencing pressing, bending, or cutting (Fig. S42, ESI[†]). The inherent safety features of Zn-Br₂ batteries make them suitable for deployment in extreme environments, such as fire detection, with a much lower risk of explosion or other hazards. As a proof-of-concept, Zn-Br₂ batteries successfully powered a drone

for forest fire detection (Fig. 6e–g and Movie S1, ESI[†]), illustrating their practical feasibility. Furthermore, as micro-batteries offer the potential to supply power to a wide array of miniaturized electronic devices, here, Zn–Br₂ micro-batteries were also developed. An in-plane interdigitated Zn–Br₂ micro-battery, based on the fully exploited hydrogel electrolyte, was prepared and integrated into a temperature and humidity meter (Fig. S43, ESI[†]). Such demonstrations of Zn–Br₂ batteries in different device architectures for a variety of applications indicate the practical feasibility and compatibility of the as-prepared electrolyte.

Conclusions

In summary, we have developed a multi-functional imidazolium bromide, MPIBr, as a predominant composite in aqueous electrolytes to simultaneously overcome the existing challenges of dendrite growth on the Zn anode and shuttle effects on the Br₂ cathode in Zn–Br₂ batteries. Systematic analysis and comprehensive characterization studies were performed to achieve an in-depth understanding of the mechanisms. The introduction of MPIBr simultaneously imparts the Zn anode with high reversibility and fast kinetics, which overcome the trade-off in traditional Zn protection strategies. This can be attributed to the H₂O-scarce IHP formed on the Zn anode with the MPI⁺ cations, which was confirmed by TEM images, local nano-FTIR spectra, ToF-SIMS, and theoretical calculations. It is also found that the MPI⁺ could effectively immobilize the generated polybromides in the cathode, thus improving the CE and life span of the Zn–Br₂ batteries. Additionally, the Br[−] anions contribute to the reconstruction of the Zn²⁺ solvation structure to form [Zn(H₂O)₅Br]⁺ with reduced desolvation energy, thus accelerating the Zn plating kinetics. Moreover, the Br[−] anions together with Zn²⁺ cations in the electrolytes enable the construction of the dual-plating Zn–Br₂ batteries without the need for active materials on both the cathode and anode. This work reveals that with rational modification on electrolyte cation and anion, all the composites in the electrolytes can be efficiently utilized to realize dendrite-free and shuttle-free high-performance metal–halide batteries. The proposed strategies for tailoring multi-functional electrolytes will inspire the advances of energy storage devices with highly desired operational safety, enhanced stability, mechanical robustness, and cost-effectiveness, so as to provide power supply for portable devices and robotics in extreme environments.

Author contributions

Y. L. and X. H. led the team and supervised the experiments. L. H., C. D., Y. L., and H. X. conceived the idea. L. H., C. D., and Z. L. prepared the electrolytes and performed electrochemical measurements. Y. Z., X. H., X. G., H. W., J. C., N. S., Q. R., and Y. Z. performed the characterization studies (FIB-SEM, AC-HAADF-STEM, XPS, AFM-IR, Raman, and FTIR) and analyzed the corresponding data. L. H. contributed to the theoretical

calculations. All authors discussed the results and agreed on the submission of the manuscript.

Data availability

The data supporting this article have been included as part of the ESI[†].

Conflicts of interest

The authors declare no conflicts of interest.

Acknowledgements

The authors would like to acknowledge the technical support from SUSTech CRF. This work was financially supported by the National Natural Science Foundation of China (62201243 and 22309124), the Guangdong Basic and Applied Basic Research Foundation (2021A1515110627), the Shenzhen Stable Support Plan Program for Higher Education Institutions Research Program (20220815153728002), the Shenzhen Science and Technology Program (RCYX20231211090432060), the China Postdoctoral Science Foundation Grant (2023M731509) and the Sichuan Provincial Natural Science Foundation (2024NSFSC1156 and 2023NSFSC1131).

References

- 1 F. Wang, O. Borodin, T. Gao, X. L. Fan, W. Sun, F. D. Han, A. Faraone, J. A. Dura, K. Xu and C. S. Wang, *Nat. Mater.*, 2018, **17**, 543–549.
- 2 Q. Zhang, Y. L. Ma, Y. Lu, L. Li, F. Wan, K. Zhang and J. Chen, *Nat. Commun.*, 2020, **11**, 4463.
- 3 J. Wu, Q. Kuang, P. Jiang, M. Huang, J. Wei, Q. Fan, Y. Dong and Y. Zhao, *Mater. Today Energy*, 2024, **42**, 101505.
- 4 S. Chen, Y. Ying, S. Wang, L. Ma, H. Huang, X. Wang, X. Jin, S. Bai and C. Zhi, *Angew. Chem., Int. Ed.*, 2023, **62**, e202301467.
- 5 C. Dai, L. Hu, X. Jin, Y. Wang, R. Wang, Y. Xiao, X. Li, X. Zhang, L. Song, Y. Han, H. Cheng, Y. Zhao, Z. Zhang, F. Liu, L. Jiang and L. Qu, *Sci. Adv.*, 2022, **8**, eabo6688.
- 6 B. Evanko, S. J. Yoo, J. Lipton, S.-E. Chun, M. Moskovits, X. Ji, S. W. Boettcher and G. D. Stucky, *Energy Environ. Sci.*, 2018, **11**, 2865–2875.
- 7 L. Gao, Z. Li, Y. Zou, S. Yin, P. Peng, Y. Shao and X. Liang, *iScience*, 2020, **23**, 101348.
- 8 S. Biswas, A. Senju, R. Mohr, T. Hodson, N. Karthikeyan, K. W. Knehr, A. G. Hsieh, X. Yang, B. E. Koel and D. A. Steingart, *Energy Environ. Sci.*, 2017, **10**, 114–120.
- 9 H. Wei, G. Qu, X. Zhang, B. Ren, S. Li, J. Jiang, Y. Yang, J. Yang, L. Zhao, H. Li, C. Zhi and Z. Liu, *Energy Environ. Sci.*, 2023, **16**, 4073–4083.
- 10 K. Xu, X. Zheng, R. Luo, J. Sun, Y. Ma, N. Chen, M. Wang, L. Song, Q. Zhao and W. Chen, *Mater. Today Energy*, 2023, **34**, 101284.

- 11 T. Li, X. Li, H. Yang, Y. Zhou, X. Li, M. Su, A. Dou, P. Zhang, X. Wu, A. Naveed, J. Sumner and Y. Liu, *Mater. Today Energy*, 2024, **40**, 101513.
- 12 Q. Zhang, Y. Ma, Y. Lu, Y. Ni, L. Lin, Z. Hao, Z. Yan, Q. Zhao and J. Chen, *J. Am. Chem. Soc.*, 2022, **144**, 18435–18443.
- 13 D. Dong, T. Wang, Y. Sun, J. Fan and Y.-C. Lu, *Nat. Sustainability*, 2023, **6**, 1474–1484.
- 14 F. Wang, J. Zhang, H. Lu, H. Zhu, Z. Chen, L. Wang, J. Yu, C. You, W. Li and J. Song, *Nat. Commun.*, 2023, **14**, 4211.
- 15 Z. Hou, T. Zhang, X. Liu, Z. Xu, J. Liu, W. Zhou, Y. Qian, H. J. Fan, D. Chao and D. Zhao, *Sci. Adv.*, 2022, **8**, eabp8960.
- 16 J.-H. Lee, Y. Byun, G. H. Jeong, C. Choi, J. Kwen, R. Kim, I. H. Kim, S. O. Kim and H.-T. Kim, *Adv. Mater.*, 2019, **31**, 1904524.
- 17 X. Li, N. Li, Z. Huang, Z. Chen, Y. Zhao, G. Liang, Q. Yang, M. Li, Q. Huang, B. Dong, J. Fan and C. Zhi, *ACS Nano*, 2021, **15**, 1718–1726.
- 18 W. Lu, P. Xu, S. Shao, T. Li, H. Zhang and X. Li, *Adv. Funct. Mater.*, 2021, **31**, 2102913.
- 19 R. Hao, S. Gu, Z. Wang, J. Chen, W. Luo, J. Hu, C. Yan, H. Yuan, G. Liu, K. Liu, C. Liu, W. Wang and Z. Lu, *Mater. Today Energy*, 2023, **33**, 101279.
- 20 J. Ke, Z. Wen, Y. Yang, R. Tang, Y. Tang, M. Ye, X. Liu, Y. Zhang and C. C. Li, *Adv. Funct. Mater.*, 2023, **33**, 2301129.
- 21 H. Wang, W. Ye, B. Yin, K. Wang, M. S. Riaz, B.-B. Xie, Y. Zhong and Y. Hu, *Angew. Chem., Int. Ed.*, 2023, **62**, e202218872.
- 22 L. Yu, J. Huang, S. Wang, L. Qi, S. Wang and C. Chen, *Adv. Mater.*, 2023, **35**, 2210789.
- 23 D. Wang, D. Lv, H. Peng, C. Wang, H. Liu, J. Yang and Y. Qian, *Angew. Chem., Int. Ed.*, 2023, **62**, e202310290.
- 24 M. Zhang, H. Hua, P. Dai, Z. He, L. Han, P. Tang, J. Yang, P. Lin, Y. Zhang, D. Zhan, J. Chen, Y. Qiao, C. C. Li, J. Zhao and Y. Yang, *Adv. Mater.*, 2023, **35**, 2208630.
- 25 Y. Lyu, J. A. Yuwono, P. Wang, Y. Wang, F. Yang, S. Liu, S. Zhang, B. Wang, K. Davey, J. Mao and Z. Guo, *Angew. Chem., Int. Ed.*, 2023, **62**, e202303011.
- 26 M. Peng, X. Tang, K. Xiao, T. Hu, K. Yuan and Y. Chen, *Angew. Chem., Int. Ed.*, 2023, **62**, e202302701.
- 27 D. Han, C. Cui, K. Zhang, Z. Wang, J. Gao, Y. Guo, Z. Zhang, S. Wu, L. Yin, Z. Weng, F. Kang and Q.-H. Yang, *Nat. Sustainability*, 2022, **5**, 205–213.
- 28 X. Wang, Y. Ying, X. Li, S. Chen, G. Gao, H. Huang and L. Ma, *Energy Environ. Sci.*, 2023, **16**, 4572–4583.
- 29 Y. Li, Z. Yu, J. Huang, Y. Wang and Y. Xia, *Angew. Chem., Int. Ed.*, 2023, **62**, e202309957.
- 30 T. Xiao, J.-L. Yang, B. Zhang, J. Wu, J. Li, W. Mai and H. J. Fan, *Angew. Chem., Int. Ed.*, 2024, **63**, e202318470.
- 31 J. Hao, L. Yuan, Y. Zhu, X. Bai, C. Ye, Y. Jiao and S.-Z. Qiao, *Angew. Chem., Int. Ed.*, 2023, **62**, e202310284.
- 32 X. Xu, M. Song, M. Li, Y. Xu, L. Sun, L. Shi, Y. Su, C. Lai and C. Wang, *Chem. Eng. J.*, 2023, **454**, 140364.
- 33 Y. Zhang, X. Zheng, K. Wu, Y. Zhang, G. Xu, M. Wu, H.-K. Liu, S.-X. Dou and C. Wu, *Nano Lett.*, 2022, **22**, 8574–8583.
- 34 D. Li, L. Cao, T. Deng, S. Liu and C. Wang, *Angew. Chem., Int. Ed.*, 2021, **60**, 13035–13041.
- 35 S. Liu, J. P. Vongsvivut, Y. Wang, R. Zhang, F. Yang, S. Zhang, K. Davey, J. Mao and Z. Guo, *Angew. Chem., Int. Ed.*, 2023, **62**, e202215600.
- 36 M. Liu, L. Yao, Y. Ji, M. Zhang, Y. Gan, Y. Cai, H. Li, W. Zhao, Y. Zhao, Z. Zou, R. Qin, Y. Wang, L. Liu, H. Liu, K. Yang, T. S. Miller, F. Pan and J. Yang, *Nano Lett.*, 2023, **23**, 541–549.
- 37 Z. Hu, F. Zhang, Y. Zhao, H. Wang, Y. Huang, F. Wu, R. Chen and L. Li, *Adv. Mater.*, 2022, **34**, 2203104.
- 38 K. Zhao, G. Fan, J. Liu, F. Liu, J. Li, X. Zhou, Y. Ni, M. Yu, Y.-M. Zhang, H. Su, Q. Liu and F. Cheng, *J. Am. Chem. Soc.*, 2022, **144**, 11129–11137.
- 39 C. Meng, W. He, L. Jiang, Y. Huang, J. Zhang, H. Liu and J.-J. Wang, *Adv. Funct. Mater.*, 2022, **32**, 2207732.
- 40 C. Li, G. Qu, X. Zhang, C. Wang and X. Xu, *Energy Environ. Mater.*, 2023, **7**, e12608.
- 41 B. Niu, Z. Li, D. Luo, X. Ma, Q. Yang, Y.-E. Liu, X. Yu, X. He, Y. Qiao and X. Wang, *Energy Environ. Sci.*, 2023, **16**, 1662–1675.
- 42 W. Zhang, Y. Dai, R. Chen, Z. Xu, J. Li, W. Zong, H. Li, Z. Li, Z. Zhang, J. Zhu, F. Guo, X. Gao, Z. Du, J. Chen, T. Wang, G. He and I. P. Parkin, *Angew. Chem., Int. Ed.*, 2023, **62**, e202212695.
- 43 D. Wang, D. Lv, H. Liu, S. Zhang, C. Wang, C. Wang, J. Yang and Y. Qian, *Angew. Chem., Int. Ed.*, 2022, **61**, e202212839.
- 44 Z. Zhao, J. Lai, D. T. Ho, Y. Lei, J. Yin, L. Chen, U. Schwingenschlögl and H. N. Alshareef, *ACS Energy Lett.*, 2023, **8**, 608–618.
- 45 C. Li, R. Kingsbury, A. S. Thind, A. Shyamsunder, T. T. Fister, R. F. Klie, K. A. Persson and L. F. Nazar, *Nat. Commun.*, 2023, **14**, 3067.
- 46 B. Liu, C. Wei, Z. Zhu, Y. Fang, Z. Bian, X. Lei, Y. Zhou, C. Tang, Y. Qian and G. Wang, *Angew. Chem., Int. Ed.*, 2022, **61**, e202212780.
- 47 Y. Liu, Y. An, L. Wu, J. Sun, F. Xiong, H. Tang, S. Chen, Y. Guo, L. Zhang, Q. An and L. Mai, *ACS Nano*, 2023, **17**, 552–560.
- 48 Y. Li, Z. Yu, J. Huang, Y. Wang and Y. Xia, *Angew. Chem., Int. Ed.*, 2023, **62**, e202309957.
- 49 X. He, J. M. Larson, H. A. Bechtel and R. Kostecki, *Nat. Commun.*, 2022, **13**, 1398.
- 50 A. S. Shaplov, E. I. Lozinskaya, I. L. Odinet, K. A. Lyssenko, S. A. Kurtova, G. I. Timofeeva, C. Iojoiu, J.-Y. Sanchez, M. J. M. Abadie, V. Y. Voytekunas and Y. S. Vygodskii, *React. Funct. Polym.*, 2008, **68**, 208–224.
- 51 G. Parveen, S. Bashir, A. Thakur, S. K. Saha, P. Banerjee and A. Kumar, *Mater. Res. Express*, 2019, **7**, 016510.
- 52 K. Li, S. R. Galle Kankanamge, T. K. Weldeghiorghis, R. Jorn, D. G. Kuroda and R. Kumar, *J. Phys. Chem. C*, 2018, **122**, 4747–4756.
- 53 W. Zhang, M. Dong, K. Jiang, D. Yang, X. Tan, S. Zhai, R. Feng, N. Chen, G. King, H. Zhang, H. Zeng, H. Li, M. Antonietti and Z. Li, *Nat. Commun.*, 2022, **13**, 5348.
- 54 D. Wang, H. Peng, S. Zhang, H. Liu, N. Wang and J. Yang, *Angew. Chem., Int. Ed.*, 2023, **62**, e202315834.
- 55 J. Holoubek, H. Liu, Z. Wu, Y. Yin, X. Xing, G. Cai, S. Yu, H. Zhou, T. A. Pascal, Z. Chen and P. Liu, *Nat. Energy*, 2021, **6**, 303–313.

- 56 Y. Zhu, Y. Cui and H. N. Alshareef, *Nano Lett.*, 2021, **21**, 1446–1453.
- 57 S. Xie, Y. Li and L. Dong, *J. Energy Chem.*, 2023, **76**, 32–40.
- 58 G. Wang, M. Zhu, G. Chen, Z. Qu, B. Kohn, U. Scheler, X. Chu, Y. Fu, O. G. Schmidt and X. Feng, *Adv. Mater.*, 2022, **34**, 2201957.
- 59 C. Wang, D. Wang, D. Lv, H. Peng, X. Song, J. Yang and Y. Qian, *Adv. Energy Mater.*, 2023, **13**, 2204388.
- 60 F. Ming, Y. Zhu, G. Huang, A.-H. Emwas, H. Liang, Y. Cui and H. N. Alshareef, *J. Am. Chem. Soc.*, 2022, **144**, 7160–7170.
- 61 W. Ling, Q. Yang, F. Mo, H. Lei, J. Wang, Y. Jiao, Y. Qiu, T. Chen and Y. Huang, *Energy Storage Mater.*, 2022, **51**, 453–464.
- 62 Y. Xu, X. Zheng, J. Sun, W. Wang, M. Wang, Y. Yuan, M. Chuai, N. Chen, H. Hu and W. Chen, *Nano Lett.*, 2022, **22**, 3298–3306.
- 63 W.-Y. Kim, H.-I. Kim, K. M. Lee, E. Shin, X. Liu, H. Moon, H. Adenusi, S. Passerini, S. K. Kwak and S.-Y. Lee, *Energy Environ. Sci.*, 2022, **15**, 5217–5228.
- 64 R. Zhao, J. Yang, X. Han, Y. Wang, Q. Ni, Z. Hu, C. Wu and Y. Bai, *Adv. Energy Mater.*, 2023, **13**, 2203542.